MATERIALS SCIENCE

Rational polyelectrolyte nanoparticles endow preosteoclast-targeted siRNA transfection for anabolic therapy of osteoporosis

Zheng Zhang[1]†, Peng Ding[2]†, Yichen Meng[1]†, Tao Lin[1], Zhanrong Zhang[1], Haoming Shu[1], Jun Ma[3], Martien Cohen Stuart[2], Yang Gao[4]*, Junyou Wang[2]*, Xuhui Zhou[1,5]*

Targeted transfection of siRNA to preosteoclasts features the potential of anti-osteoporosis, yet challenge arises from the development of satisfied delivery vehicles. Here, we design a rational core-shell nanoparticle (NP) composed of cationic and responsive core for controlled load and release of small interfering RNA (siRNA) and compatible polyethylene glycol shell modified with alendronate for enhanced circulation and bone-targeted delivery of siRNA. The designed NPs perform well on transfection of an active siRNA (siDcstamp) that interferes Dcstamp mRNA expression, leading to impeded preosteoclast fusion and bone resorption, as well as promoted osteogenesis. In vivo results corroborate the abundant siDcstamp accumulation on bone surfaces and the enhanced trabecular bone mass volume and microstructure in treating osteoporotic OVX mice by rebalancing bone resorption, formation, and vascularization. Our study validates the hypothesis that satisfied transfection of siRNA enables preserved preosteoclasts that regulate bone resorption and formation simultaneously as potential anabolic treatment for osteoporosis.

INTRODUCTION

Osteoporosis is a widespread condition affecting millions of people and causing billions of dollars of annual health care costs (*1*, *2*). It finds its origin in disturbed bone remodeling. Bone remodeling begins with resorption of old bone by osteoclasts derived from hemopoietic stem cells, which is followed by new bone formation by osteoblasts originating from bone marrow mesenchymal stem cells (BMSCs) (*3*). The cellular basis of osteoporosis is excessive osteoclastogenesis, along with diminished osteogenesis and angiogenesis. At present, the most common clinical treatments to inhibit pathological bone loss rely on antiresorptive drugs such as bisphosphonates (*4*). Unfortunately, these treatments do not restore the balance between bone formation and breakdown and are associated with clinical complications such as atypical fractures and decreasing bone strength upon long-term use (*5*, *6*). Therefore, developing an alternative strategy for a satisfactory osteoporosis therapy is highly desirable. As a starting point, one could make use of the fact that mononuclear preosteoclasts with a weak resorption function are essential precursors for the formation of mature osteoclasts (*7*). Moreover, recent studies have revealed that preosteoclasts can also secrete the platelet-derived growth factor BB (PDGF-BB) that induces angiogenesis of type H blood vessels (CD31^hiEndomucin^hi) and recruits osteoblast progenitors (*1*, *8*). Correspondingly, a prospective anti-osteoporosis strategy that has emerged is to block the maturation of preosteoclasts; it not only causes suppression of bone resorption but also promotes vascularization and bone formation (*9*, *10*).

In recent decades, therapies based on nucleic acids, in particular, siRNA, are developing rapidly (*11*). Small interfering RNAs (siRNAs) are double-stranded RNAs with a length of 21 to 23 nucleotides, which can effectively induce cleavage and degradation of mRNA by forming multiprotein RNA-inducing silencing complexes (RISC) (*12*). Transfection of siRNAs is supposed to be a promising approach for the preservation of preosteoclasts; unfortunately, transfection is often not successful, suffering from different limitations at this stage. One of the challenges is the development of an appropriate delivery system that can solve the problems associated with naked siRNA, such as its low stability in serum, immunogenic responses, and low cellular uptake (*13*). Particularly, osteoclast progenitors derived from hemopoietic stem cells show low uptake efficiency and high susceptibility to cytotoxic effects of transfection agents (*14*). Although a variety of nanocarriers, including polymers, lipid nanoparticles (NPs), dendrimers, and exosomes, have been proposed for siRNA delivery (*11*, *15*–*19*), finding one that endows sufficient siRNA delivery to preosteoclasts remains a challenge.

In this work, we attempt a rational design of transfection vehicle. To be successful, an RNA transfection vehicle must satisfy multiple requirements including sufficient encapsulation and protection of RNA, as well as long circulation, targeted delivery, and controlled release of RNA. Our design deals with these criteria in the following way. For uptake, we make use of the anionic character of RNA, which will spontaneously associate with positive charges; this can be realized by a particle having a cross-linked cationic polymer as its core. The core is covered with a neutral shell of inert, biocompatible polyethylene glycol (PEG) chains, which give the particle stealth character and provide the protection against enzymatic attack of RNA. Bone cell targeting is achieved by end-attaching a chemical

¹Department of Orthopedics, Changzheng Hospital, Second Military Medical University (Naval Medical University), Shanghai 200003, China. ²State-Key Laboratory of Chemical Engineering, East China University of Science and Technology, Shanghai 200237, China. ³Department of Orthopedics, Shanghai General Hospital (Shanghai First People's Hospital), Shanghai Jiao Tong University School of Medicine, Shanghai 200080, China. ⁴Department of Orthopedics, The Fourth Medical Center, Chinese People's Liberation Army General Hospital, Beijing 100048, China. ⁵Translational research center of orthopedics, Shanghai General Hospital (Shanghai First People's Hospital), Shanghai Jiao Tong University School of Medicine, Shanghai 200080, China.
†These authors contributed equally to this work.
*Corresponding author. Email: zhouxuhui@smmu.edu.cn (X.Z.); junyouwang@ecust.edu.cn (J.W.); gaoyangspine@qq.com (Y.G.)

group to the PEG chains that specifically binds to bone. Alendronate was chosen as the navigation group because of its high affinity to hydroxyapatite, which is the main mineral component of bone (*20*). Last, release of the RNA inside the cell is achieved by selecting a cross-linker that contains an internal disulfide group, which is known to be readily degraded after endocytosis by the intracellular reducing agent glutathione (*21*).

An NP made according to this design integrates all the necessary functionalities to be successful as transfection vehicle, by enabling enough siRNA transfection to effectively impede the fusion of preosteoclasts and hence synergistically promoting bone formation and vascularization. In the present study, we put these ideas to the test, first preparing the particles according to the design and then investigating, both in vitro and in vivo, how they perform as transfection vehicles of siRNA and anti-osteoporosis medication.

RESULTS

The dendrocyte-expressed seven transmembrane protein (DCSTAMP) is a critical regulator for the cell fusion of preosteoclasts and the formation of highly functional osteoclasts (*22, 23*). Note that DCSTAMP is barely expressed in BMSCs and osteoblast lineage cells and therefore displays no functions in these cells. In this work, we design an active siRNA that enables silencing the expression of Dcstamp (siDcstamp; table S1) so that fusion of the preosteoclasts is suppressed. A nonfunctional siRNA (no function, defined as siNC) was selected as negative control. As for the delivery vehicle, we choose a type of "soft" NP, which features both hydrogel and polyelectrolyte properties (*24–26*). It is a core-shell polyelectrolyte NP, with a gel-like particle core consisting of a cross-linked cationic polymer that provides abundant positive charges and acts as a hydrated pocket that can carry and protect the anionic siRNA. The particle shell is composed of biocompatible PEG block end-functionalized with alendronate, which serves as the bone cell–targeting group. The role of the shell is to ensure both long circulation time and specific delivery of siRNA to the surface of bone cells. Last, we select a redox-responsive cross-linker so that the NP can dissociate and release its siRNA cargo upon exposure to glutathione present in the cell (Fig. 1).

We first discuss the synthesis of the polyelectrolytes NPs and then make a detailed study of their capability to load and deliver siRNA. After that, we investigate by both in vitro and in vivo measurements the synergistic effects of the loaded particles: whether they block the fusion of preosteoclast fusion and promote bone formation and vascularization.

Synthesis of polyelectrolyte NPs and loading of siRNA

As shown in Fig. 1A, the core-shell polyelectrolyte NPs were synthesized on the basis of our recently developed strategy involving cooperative electrostatic assembly and polymerization (*27, 28*). We first modified a PEG block [weight-average molecular weight (M_w) = 5000; fig. S1] with an alendronate (AD) group on one end and a RAFT agent [reversible addition-fragmentation chain transfer agent (CTA)] on the other end. The chain growth (core formation) starts on the RAFT agent side and leaves the alendronate group on the particle surface for bone targeting delivery. Specifically, in the presence of the AD-PEG-CTA and anionic PAA (polyacrylic acid) as template, cationic METAC {[2-(methacryloyloxy) ethyl] trimethylammonium chloride} monomers were polymerized together with

BAC [*N,N*-bis(acryloyl) cystamine] cross-linker. Upon polymerization under ultraviolet (UV) light, poly-METAC (PMETAC) grows from the AD-PEG-CTA together with a BAC cross-linker, forming an NP due to charge complexation with the PAA chains, which act as template. The successful polymerization is proven by ^{1}H nuclear magnetic resonance (NMR; fig. S2). The increased light scattering intensity after polymerization indicates the formation of micelle-like NPs with a hydrodynamic radius of about 82 nm and a narrow size distribution (Fig. 2, A and B). The core of the "micelles" consists of polyelectrolyte complex between the cationic PMETAC network and the anionic PAA template. The latter is removed by dissociating the complex in high salt concentration, as evidenced by the decay of light scattering intensity (Fig. 2A). Subsequent filtration with a semipermeable membrane under centrifugal force allows it to obtain purified core-shell NPs with cationic PMETAC network core surrounded by PEG chains (Fig. 2B and fig. S2).

We next varied the salt concentration and cross-linker fraction during the polymerization to obtain a series of NPs with different sizes and degrees of cross-linking (Fig. 2C) (*29, 30*). Since our strategy relies on charge-driven assembly during polymerization, salt has an effect on the final particle size. We controlled the added NaCl concentrations at 0, 30, and 45 mM for preparing NP1 to NP3 under the fixed BAC fraction of 20%, and obtained NPs display increased hydrodynamic radii from 87 to 200 nm. It seems that increasing the salt concentrations leads to declined charge interactions and consequently enhanced mobility of the charged building blocks, which is favorable for creating bigger NPs (*31, 32*). Labels NP4 and NP5 are particles with the same size but have increased cross-linker fractions of 30 and 40%, respectively. All of the NPs display narrow size distributions and spherical morphology (Fig. 2, C to E, and fig. S3).

To confirm that the disulfide bond in the cross-linker allows degradation of the NPs, we prepared an extra batch of NPs MBA-NP2 with the cross-linker MBA (*N,N*′-methylenebisacrylamide; without disulfide bonds) and exposed these, as well as the BAC-containing particles, to 10 mM GSH [glutathione (reduced form)] solution. As shown in Fig. 2F, the NPs with the BAC cross-linker dissociate completely within a few minutes, as indicated by the strong decay of light scattering intensity, in contrast to the NPs containing MBA cross-linker, which remain intact. Since the intracellular GSH concentration is comparable to the test concentration, this response implies that the designed NPs are very likely to dissociate and release siRNA after endocytosis (*33*).

Next, NP2 was selected for a detailed investigation of loading and intracellular delivery of siRNA. The toxicity of the NPs was estimated by CCK-8 assays. The results consistently exhibited cell viability up to a particle concentration of 150 μg/ml (fig. S4A). Using the control siNC, we investigated the effects of mixing ratio on the formation of NP2-siNC complexes. The siNC concentration was fixed at 1 μg/ml, and the NP2 concentrations were varied from 1 to 80 μg/ml, corresponding to NP2/siNC weight ratios of 1:1 to 80:1. The successful loading of siNC was confirmed by agarose gel electrophoresis, where a progressive decay of the amount of mobile siNC with increasing NP2/siNC ratio (Fig. 3A) can be clearly seen. Full complexation was found at a ratio of 20:1 as evidenced by the complete vanishing of mobile siNC; we therefore chose this ratio for all subsequent experiments.

To test the stability of entrapped nucleic acid against serum-mediated degradation, naked siNC and NP2-siNC complexes were
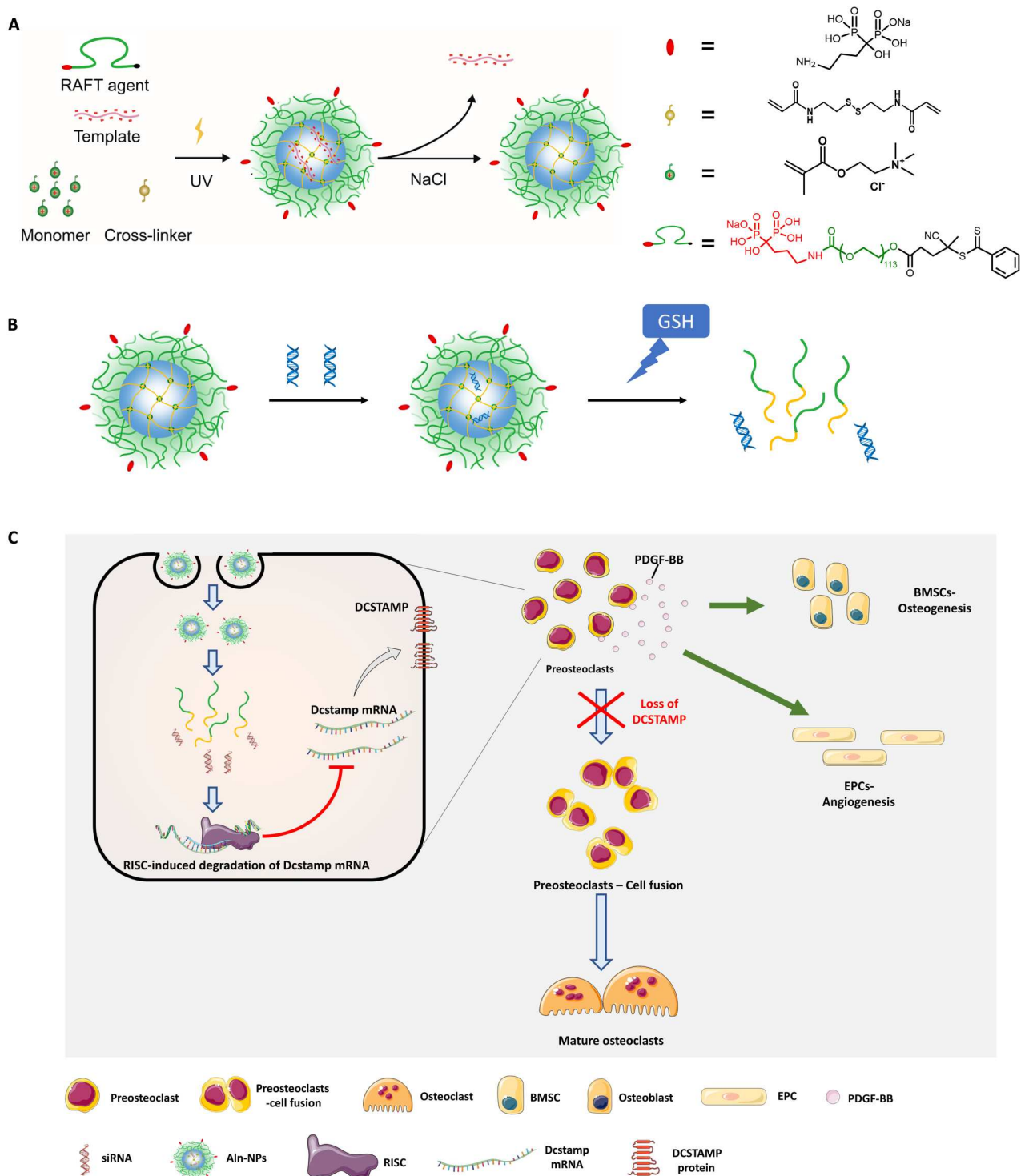
Fig. 1. Schematic diagram showing the synthesis of polyelectrolyte NPs. (**A**) Preparation of core-shell polyelectrolyte NPs. Chemical structures of alendronate, METAC monomer, BAC cross-linker, and AD-PEG-CTA. (**B**) Loading siRNA, redox response of the NP, and the triggered release of siRNA. (**C**) Proposed functionality of polyelectrolyte NPs. siRNA targeting Dcstamp (siDcstamp) is transfected into BMMs/preosteoclasts by the NPs, which then recruit RISC to degrade Dcstamp mRNA. The decrease of DCSTAMP protein blocks the cell-cell fusion of the preosteoclasts. The preserved preosteoclasts lead to enhanced osteogenesis of BMSCs and angiogenesis of endothelial progenitor cells (EPCs) via PDGF-BB.
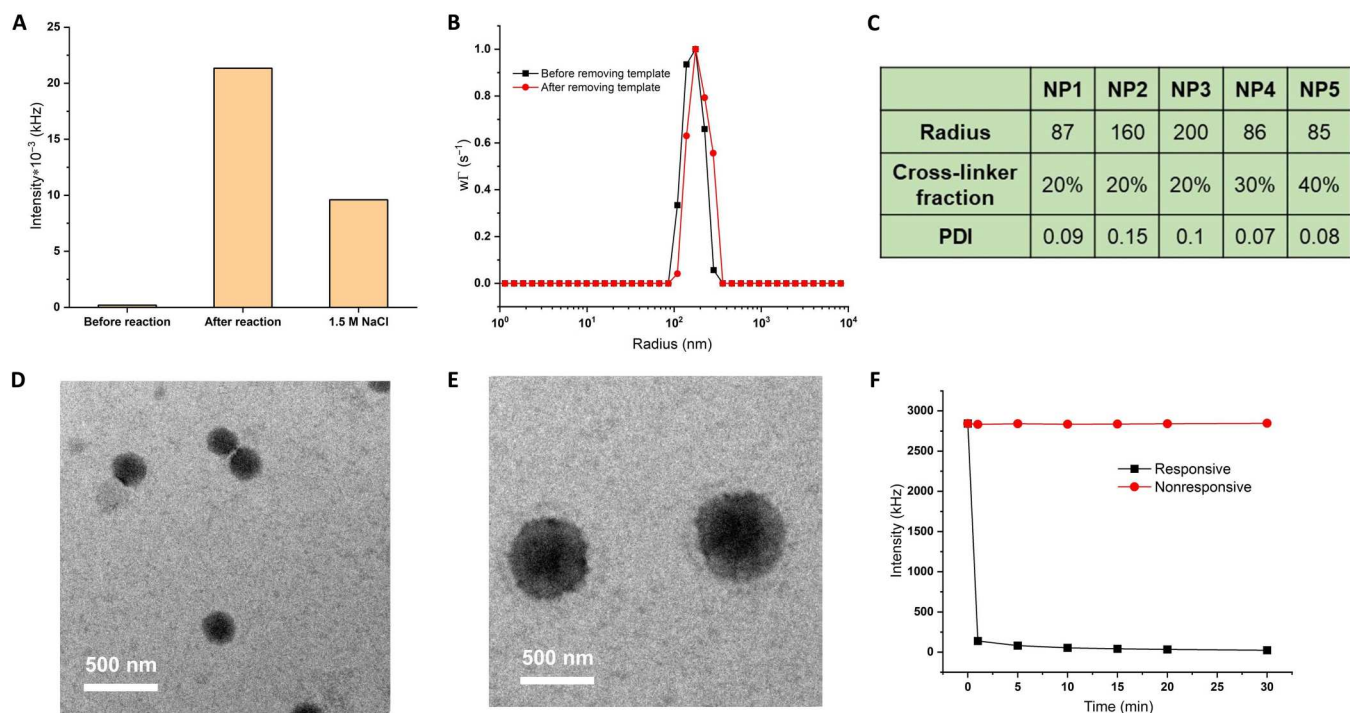
Fig. 2. Synthesis of polyelectrolyte NPs. (**A**) Light scattering intensity of mixture before and after polymerization and the reaction mixture with added 1.5 M NaCl. (**B**) Size and size distribution of the micelles before and after removing the template. (**C**) Obtained core-shell polyelectrolyte NPs with various sizes (NP1 to NP3) and cross-link degrees (NP4 to NP5). (**D** and **E**) Transmission electron microscopy images of representative NP1 and NP3. (**F**) Variations of light scattering intensity upon addition of 10 mM GSH to redox-responsive NP2 and nonresponsive MBA-NP2.

both incubated in fetal bovine serum (FBS). Electrophoretic assays revealed that the band of naked siNC disappears after 6-hour incubation, whereas the bands of siNC-NP2 complexes still exist after incubation with serum even after 48 hours (Fig. 3B).

Using the fixed NP/siNC ratio of 20:1, we compared the delivery capability of NP1 to NP5. Flow cytometry analysis (Fig. 3C) and transfection efficiency (Fig. 3D) indicated that NP2 exhibited a maximum transfection of siNC up to nearly 100%, which was consistent with the intracellular release and enrichment of siNC (tagged with FAM dye) seen in the fluorescence images (Fig. 3E). Varying the NP size (NP1 to NP3) had moderate effects on the transfection efficiency, but increasing the degree of cross-linking (NP4 and NP5) caused a reduction of transfection efficiency. We further investigated the silencing efficiency of siRNA by real-time quantitative polymerase chain reaction (RT-qPCR). As shown in fig. S4B, the NP2-siNC complexes caused hardly any inhibition of the expression of Gapdh mRNA, while NP2-siGapdh (positive control siRNA) reduced Gapdh expression in a dose-dependent manner. Results so far demonstrate that the designed NPs are a biocompatible platform that enables efficient loading and intracellular delivery of siRNA.

Investigation of siRNA transfection and therapeutic effects in vitro
Inhibition of preosteoclast fusion by siDcstamp transfection
The following study explored whether the NP-induced transfection of siRNA can successfully impede preosteoclast fusion and promote vascularization and bone formation synergistically. NP2 was applied as the delivery platform, and Dcstamp siRNA (siDcstamp)

was selected, with siNC as the negative control. To distinguish the targeting and inhibition effects of the alendronate group (4), we also prepared an NP2 sample without alendronate groups, labeled as *NP2. The NP/siRNA ratio was fixed at 20:1, with an siRNA dosage of 1 μg/ml (fig. S5). First, Dcstamp mRNA and DCSTAMP protein expression were estimated, as well as the osteoclast number and size (Fig. 4, A to D). Our results showed that *NP2-siNC had no effects, neither on mRNA and DCSTAMP protein expression nor on osteoclastogenesis. The NP2-siNC complexes caused a moderate reduction of mRNA and protein expression, as well as the osteoclast number and size. This effect was assigned to the inhibition of osteoclastogenesis by alendronate, which induces preosteoclast apoptosis and impairs PDGF-BB secretion via peroxisomal dysfunction and endoplasmic reticulum stress (34). In contrast, both *NP2-siDcstamp and NP2-siDcstamp complexes induced strong suppression of marker expression (fig. S6) and osteoclastogenesis, confirming the anti-osteoporosis function of the designed Dcstamp siRNA. The NP2-siDcstamp group displayed a stronger inhibition than *NP2-siDcstamp, due to the combined effect of both siDcstamp and alendronate (Fig. 4, A to D).

Next, preosteoclast fusion and bone resorption were estimated on the basis of tracing the F-actin ring, the membrane merge rate, and resorption area. Phalloidin staining was applied to investigate the F-actin ring, which is an indicator of mature and functional osteoclasts. A double fluorescence method was used, by culturing two groups of bone marrow monocytes [BMMs; labeled with DiI (red) and Hoechst (blue), respectively] to evaluate preosteoclast fusion and of membrane merge rate. The BMMs were seeded onto Osteo-Assay plates to estimate the bone resorption after transfection by
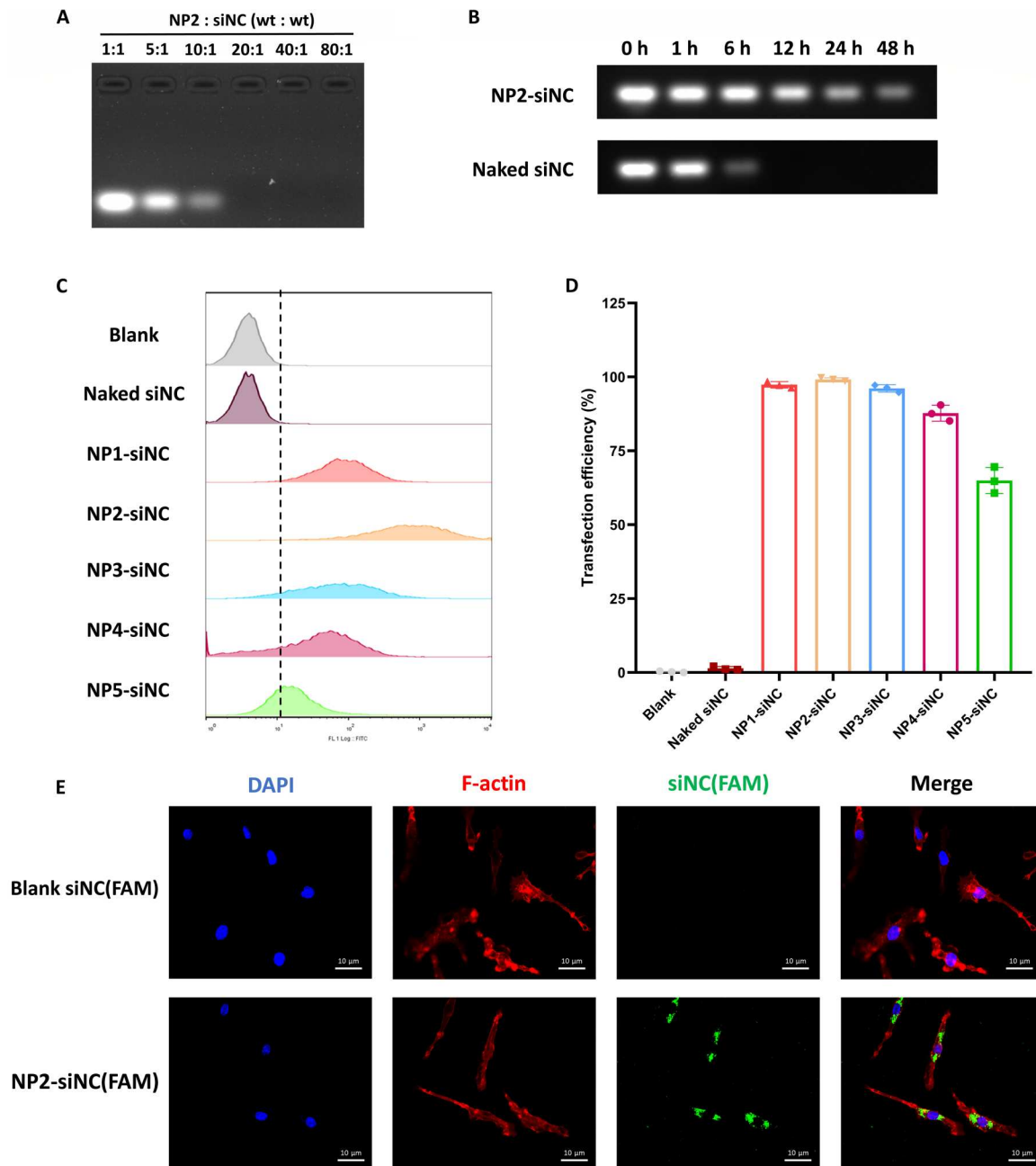
Fig. 3. The loading and intracellular transfection of siRNA by NPs. (**A**) Loading of siNC and NPs evaluated by electrophoretic mobility assays at different NP/siNC ratios. (**B**) Serum stability of naked and NP-loaded siNC at different time points. (**C** and **D**) Flow cytometry analysis (C) and corresponding transfection efficiency (D) of NPs with different sizes and cross-link degrees. (**E**) Uptake of NP2-siNC by BMMs shown by confocal images. The concentration of siRNA was fixed at 1 µg/ml, and the NP/siRNA ratio was at 20:1.

different NP-siRNA complexes. As shown in Fig. 4 (E to J), the *NP2-siNC and NP2-siNC groups showed, respectively, no and moderate inhibition of F-actin ring formation, membrane merge rate, and bone resorption. As expected, siDcstamp transfected by both *NP2 and NP2 led to remarkable suppression of preosteoclast fusion and bone resorption; the latter one showed stronger suppression than the former one. In view of these findings, we conclude that the successful transfection of siDcstamp by our designed NPs impedes osteoclastogenesis by blocking fusion of preosteoclasts.

Promotion of osteogenesis and angiogenesis by siDcstamp transfection

It has been reported that preosteoclasts can induce vascularization by secreting PDGF-BB (*1*, *35*). To investigate whether preosteoclasts preserved by siDcstamp exert a beneficial effect on angiogenesis, co-culture systems of epithelium progenitor cells (EPCs)/BMMs were prepared. BMMs were cultured in osteoclastic medium with M-SCF (macrophage colony-stimulating factor; 30 ng/ml) and RANKL (receptor activator of nuclear factor κB ligand; 80 ng/ml) for 5 days. We
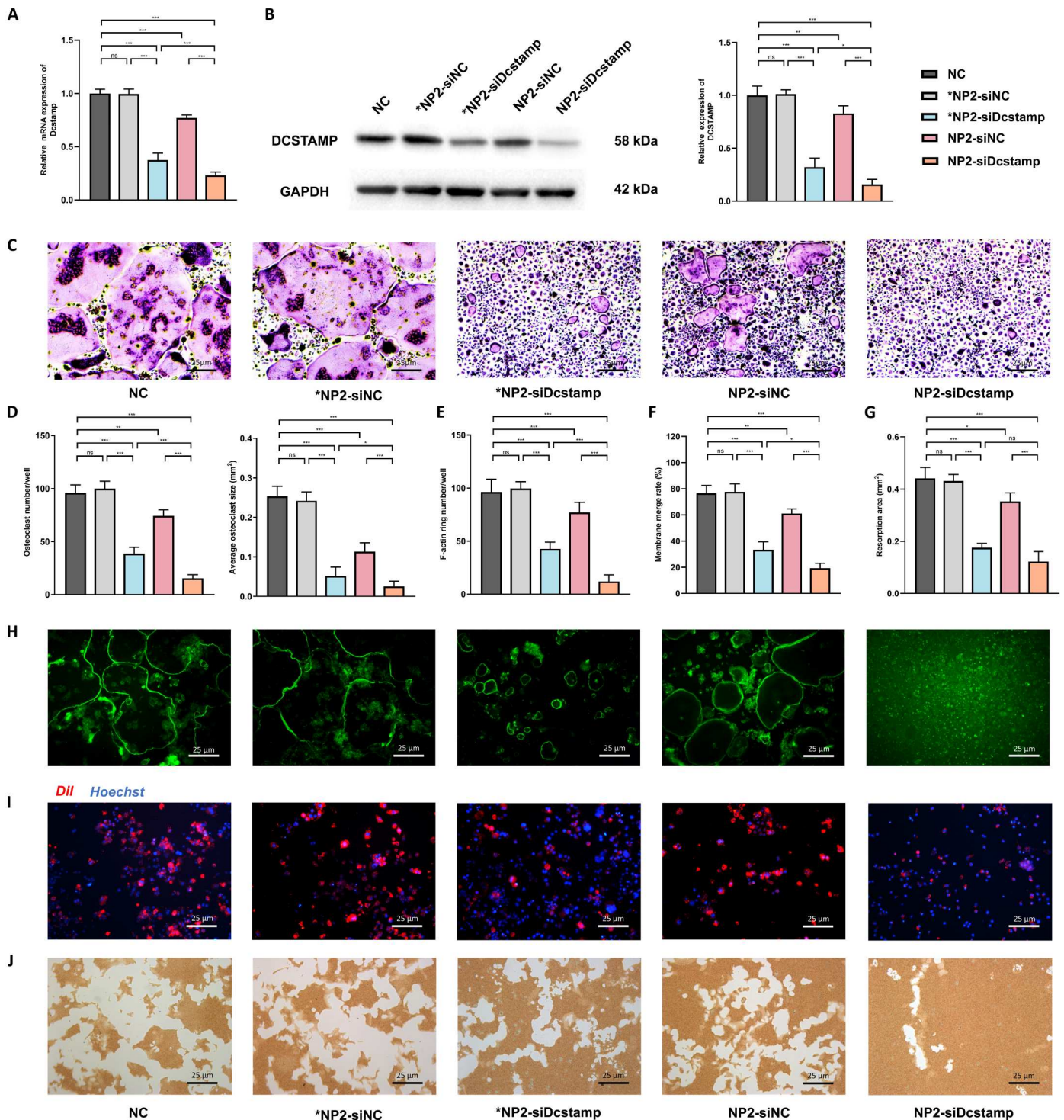
Fig. 4. Transfection of siDcstamp impedes preosteoclast fusion and bone resorption. (**A**) Dcstamp mRNA expression of BMMs transfected with different NP2-siRNA complexes in osteoclastic condition (with RANKL); $n = 3$ per group. (**B**) Protein levels of DCSTAMP measured by Western blot; $n = 3$ per group. (**C**) Effects of different groups on osteoclast differentiation measured by TRAP staining. (**D**) Quantification of osteoclast numbers and average size per well; $n = 5$ per group. (**E** and **H**) Quantification of F-actin rings of different groups; $n = 5$ per group. (**F** and **I**) Cell-cell fusion assay of preosteoclasts in different groups and quantification of membrane merge rate; $n = 3$ per group. (**G** and **J**) Pit formation assay of osteoclasts in different groups and quantification of the resorption area; $n = 3$ per group. Data are expressed as means ± SD. ns, no significance; *$P < 0.05$; **$P < 0.01$; ***$P < 0.001$. Scale bar, 25 μm.
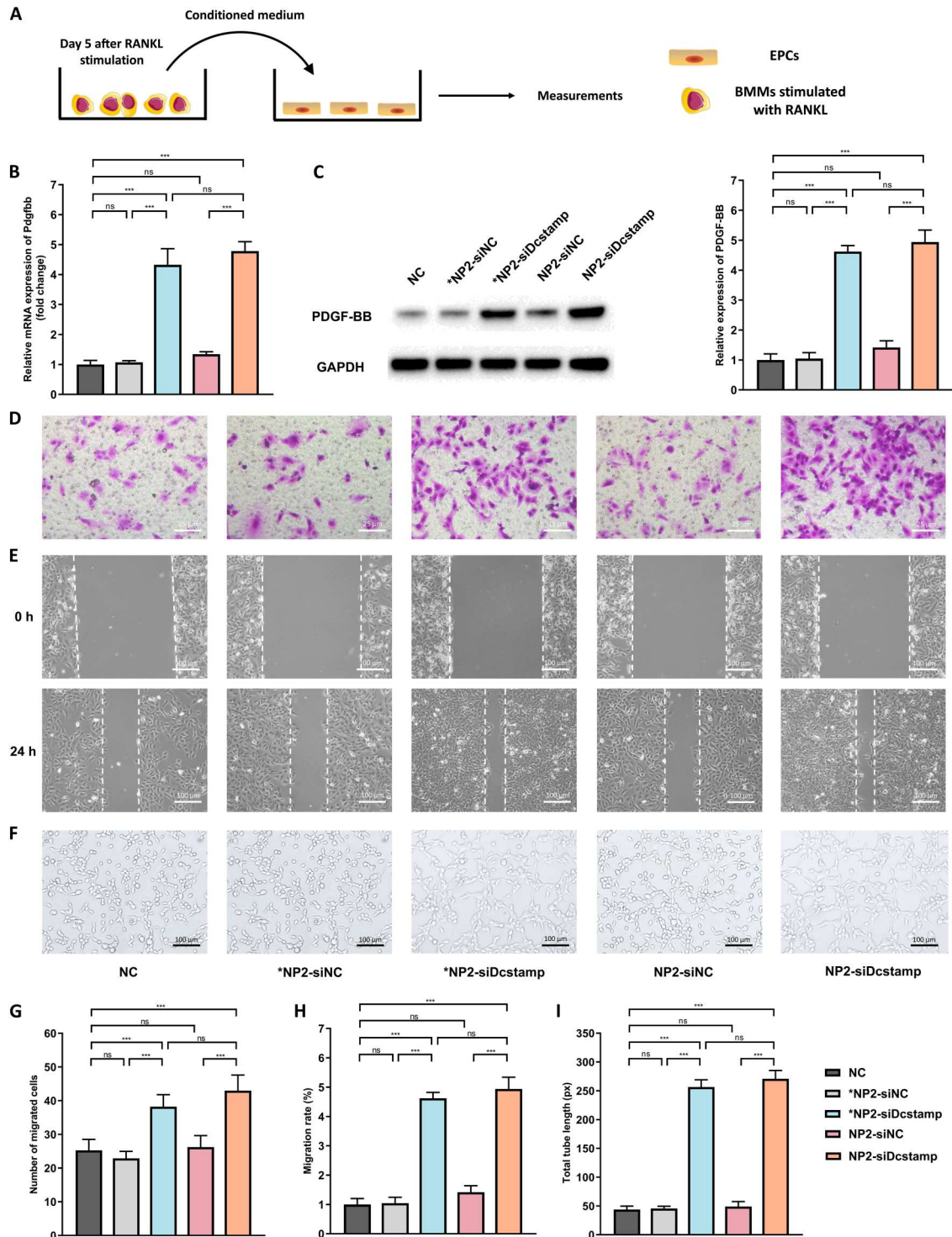
Fig. 5. Transfection of siDcstamp promotes angiogenesis. (**A**) Illustrating the coculture of EPCs and BMMs under the stimulation of RANKL. (**B** and **C**) Relative mRNA levels of Pdgf-bb (B) and protein levels of PDGF-BB (C) of BMMs in different groups; $n = 3$ per group. (**D** and **G**) EPC migration capacity in different groups measured by the transwell migration assay; $n = 3$ per group. (**E** and **H**) EPC motility in different groups evaluated by the scratch wound assay; $n = 3$ per group. (**F** and **I**) Tube formation of EPCs on Matrigel in different groups; $n = 3$ per group. Data are expressed as means ± SD. ns, no significance; *$P < 0.05$; **$P < 0.01$; ***$P < 0.001$.

then collected the osteoclast medium and mixed it with normal medium at a ratio of 1:2 as conditioned medium (CM) to culture EPCs for further experiments (Fig. 5A). After siDcstamp transfection using our designed NPs, the mRNA levels of Pdgf-bb and protein levels of PDGF-BB in the BMMs increased substantially when compared to the NC group (Fig. 5, B and C). As evidenced by the transwell assay and scratch wound assay, both the *NP2-siDcstamp and the NP2-siDcstamp complexes notably promoted motility and ability to migrate to the EPCs (Fig. 5, D to H), as well as the formation of capillary tube-like structures on Matrigel (Fig. 5, F and I). This result suggested that the alendronate groups hardly influence the transfection of siDcstamp. Moreover, NP2-siNC in this test barely promoted the mRNA level and PDGF-BB protein, as well as CM from BMM and EPC mobility. The negligible effect of alendronate here is different from the results regarding the blocking of preosteoclast fusion in Fig. 4. For this reason, we attribute the achieved preservation of preosteoclasts to the transfected siDcstamp, which demonstrates a different way on suppression of preosteoclast with alendronate. Moreover, to check whether separated siDcstamp or NP2 can directly influence angiogenesis, CM was generated from BMMs cultured in medium without RANKL (fig. S7A). The expression of PDGF-BB mRNA and proteins, and the migration capacity and tube formation ability of EPC exhibited subtle differences in the different groups of BMMs (fig. S7, B to G). This control test confirmed that the promotion of EPC angiogenesis by preserving preosteoclast arises from the successful transfection of siDcstamp by our designed transfection vehicles.

Preosteoclasts have been reported to promote osteoblast differentiation by activating the PDGF receptor β (PDGFRβ)–phosphatidylinositol 3-kinase (PI3K)–AKT pathway (9, 36). Therefore, we further investigate the effects of siDcstamp transfection on the coupling of osteogenesis. To do so, BMSCs and BMMs were seeded at the upper and bottom chambers of transwell plates as a coculture system. Cells were cultured in osteogenic medium with M-SCF (30 ng/ml) and RANKL (50 ng/ml) for 6 days, and BMSCs were harvested for measurements (Fig. 6A). A notable increase in alkaline phosphatase (ALP) activity was observed in groups treated with transfected siDcstamp with both *NP2 and NP2, as compared to the NC group (Fig. 6, B and C). Consistently, the transcriptional levels of osteogenic markers including Runx2, Alp, and Bglap [the gene coding for Osteocalcin (OCN)] and the corresponding proteins were up-regulated by treatments of siDcstamp delivered by *NP2 and NP2 (Fig. 6, D to H). We further used immunofluorescence to visualize OCN protein in cocultured BMSCs, which also revealed that OCN expression was augmented by *NP2-siDcstamp and NP2-siDcstamp complexes (Fig. 6, I and J). To eliminate the possibility that siDcstamp or NPs could promote osteogenesis directly, BMSCs and BMMs were cocultured in osteogenic medium without RANKL for 6 days (fig. S8A). As expected, ALP activity and mRNA levels of Runx2, Alp, and Bglap showed no substantial difference among the different groups (fig. S8, B to D). These findings implied that alendronate has limited effects on preserving preosteoclasts, and the facilitation of osteogenic differentiation of BMSCs by preserving preosteoclasts comes from the transfected siDcstamp.

Investigation of siRNA transfection and therapeutic effects in vivo

Inspired by the promising results from in vitro investigation, the following studies turned to explore the siRNA transfection and therapeutic effects in vivo. We started with tracing the biodistribution of the NP-siRNA complexes and estimating the toxicity of the designed NPs. An ovariectomy (OVX) mice model was developed to fully investigate the therapeutic effects of siDcstamp against pathological bone loss.

Biodistribution and compatibility of NP2-siRNA complexes

To test whether the designed NPs are capable to deliver siRNA to bone surfaces in vivo, we selected Cy3-labeled siDcstamp for fluorescence imaging studies. Both *NP2-siDcstamp and NP2-siDcstamp complexes were injected intravenously to mice, and an in vivo imaging system was used to identify the organ distribution of Cy3 fluorescence. For the naked siDcstamp, and at 8 hours after injection, the highest fluorescence intensity was observed in the kidneys, indicating a quick clearing of the naked siRNA from circulation (Fig. 7A). The *NP2-siDcstamp complexes led to enhanced accumulation in lungs and liver but were barely collected in bones (Fig. 7A). Only the NP2-siDcstamp complexes displayed higher fluorescence intensity at femurs, tibias, and spine (Fig. 7A). The favorable accumulation on bone surfaces was assigned to the targeting by alendronate present on NP2. To confirm siDcstamp transfection into preosteoclasts, tartrate-resistant acid phosphatase (TRAP) was labeled by immunofluorescence (green) on femoral sections. In line with in vivo imaging system (IVIS) imaging, there was only occasional fluorescence (red) on bone surfaces when naked siDcstamp or *NP-siDcstamp complexes were injected (Fig. 7B). In contrast, preosteoclasts/osteoclasts were abundantly colabeled with siRNA delivered by NP2 (Fig. 7B). Moreover, we further estimated the in vivo biocompatibility of the NPs and siDcstamp by administration of *NP2 and NP2 every other day for 3 weeks. Organs including heart, lungs, liver, spleen, and kidneys were then harvested, and histomorphometry results showed feeble alterations (Fig. 7C), which validate the good biocompatibility of the NPs. Together, the results in this part demonstrate that NP2 can target bone cell surfaces and deliver siRNA to preosteoclasts without inducing systemic toxicity.

Therapeutic effects of NP2-siDcstamp in OVX mice

Last, the following study explored the therapeutic effects of NP2-siDcstamp in the osteoporotic OVX mice model. In this part, *NP2 without alendronate was not used because of its failure to specifically deliver to bone. Only NP2 was applied as the delivery platform. One week after OVX surgery, the mice were intraperitoneally injected with NP2-siNC and NP2-siDcstamp complexes, twice a week during 5 weeks. Then, the mice were sacrificed, and the femurs, spine, and sera were collected for examination. As shown in Fig. 8 (A to G), serious trabecular femoral bone loss was observed in OVX mice shown by micro–computed tomography (μCT) and hematoxylin and eosin (H&E) staining. Treatment with NP2-siNC complexes hardly reversed the osteopenia phenotype of OVX mice, but the NP2-siDcstamp treatment induced substantial augmentation of the bone volume fraction (BV/TV) and trabecular number (Tb.N) (even higher than the Con group; Fig. 8, A to C), as well as a notable decrease of trabecular space (Tb.Sp; Fig. 8D). Consistently, the trabecular area (Tb.Ar) from H&E staining also
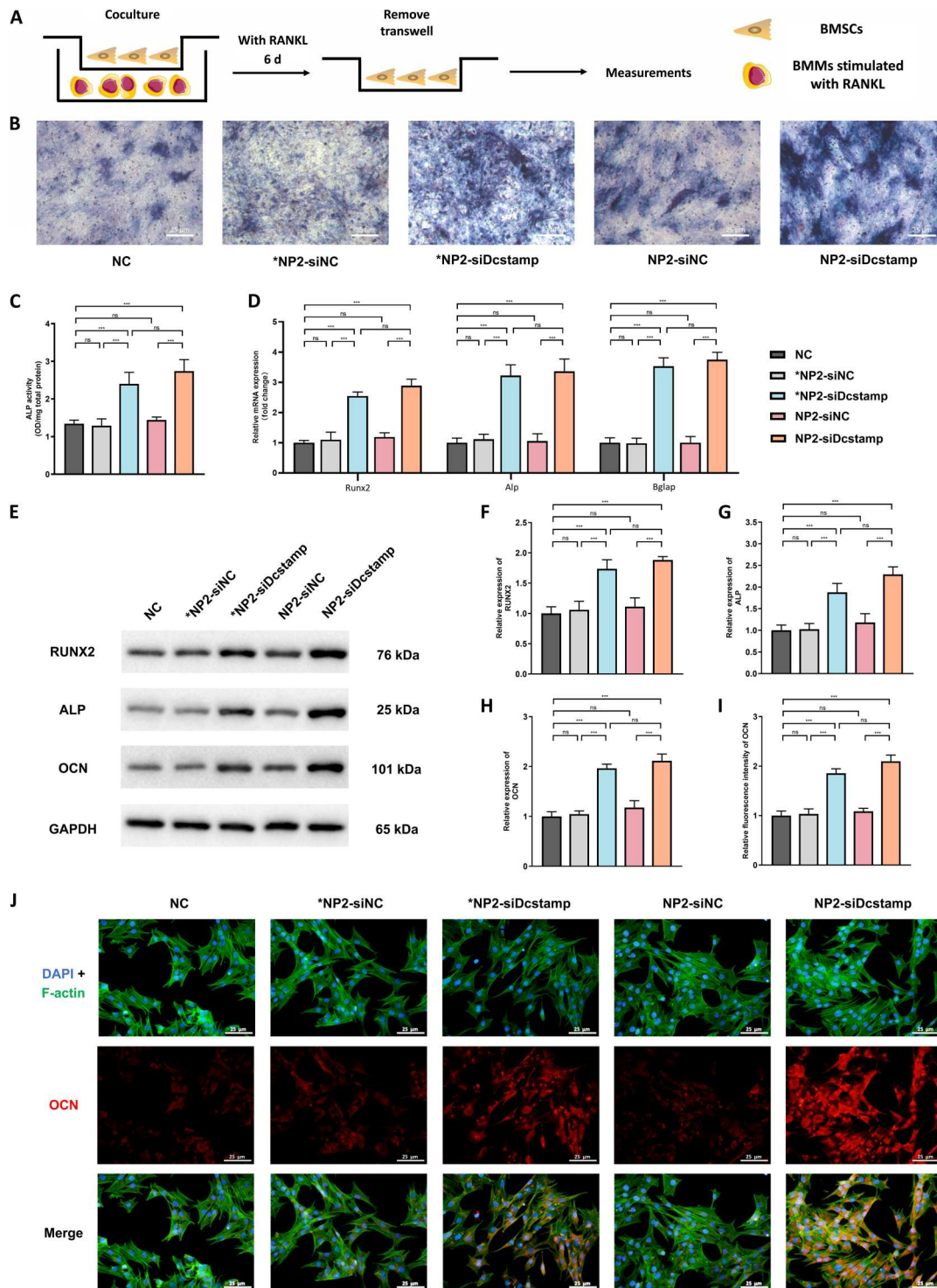
Fig. 6. Transfection of siDcstamp promotes osteogenesis. (**A**) Illustrating the coculture of BMSCs and BMMs under the stimulation of RANKL. (**B** and **C**) ALP staining (B) and quantification of ALP activity (C) of different groups; $n = 4$ per group. (**D** to **H**) Relative mRNA levels (D) and corresponding proteins (E to H) of osteogenic markers including Runx2, Alp, and Bglap; $n = 3$ per group. (**I**) Quantification of OCN fluorescence intensity in different groups; $n = 3$ per group. (**J**) Representative immunofluorescence images of OCN (red) in different groups. Data are expressed as means ± SD. ns, no significance; *$P < 0.05$; **$P < 0.01$; ***$P < 0.001$.
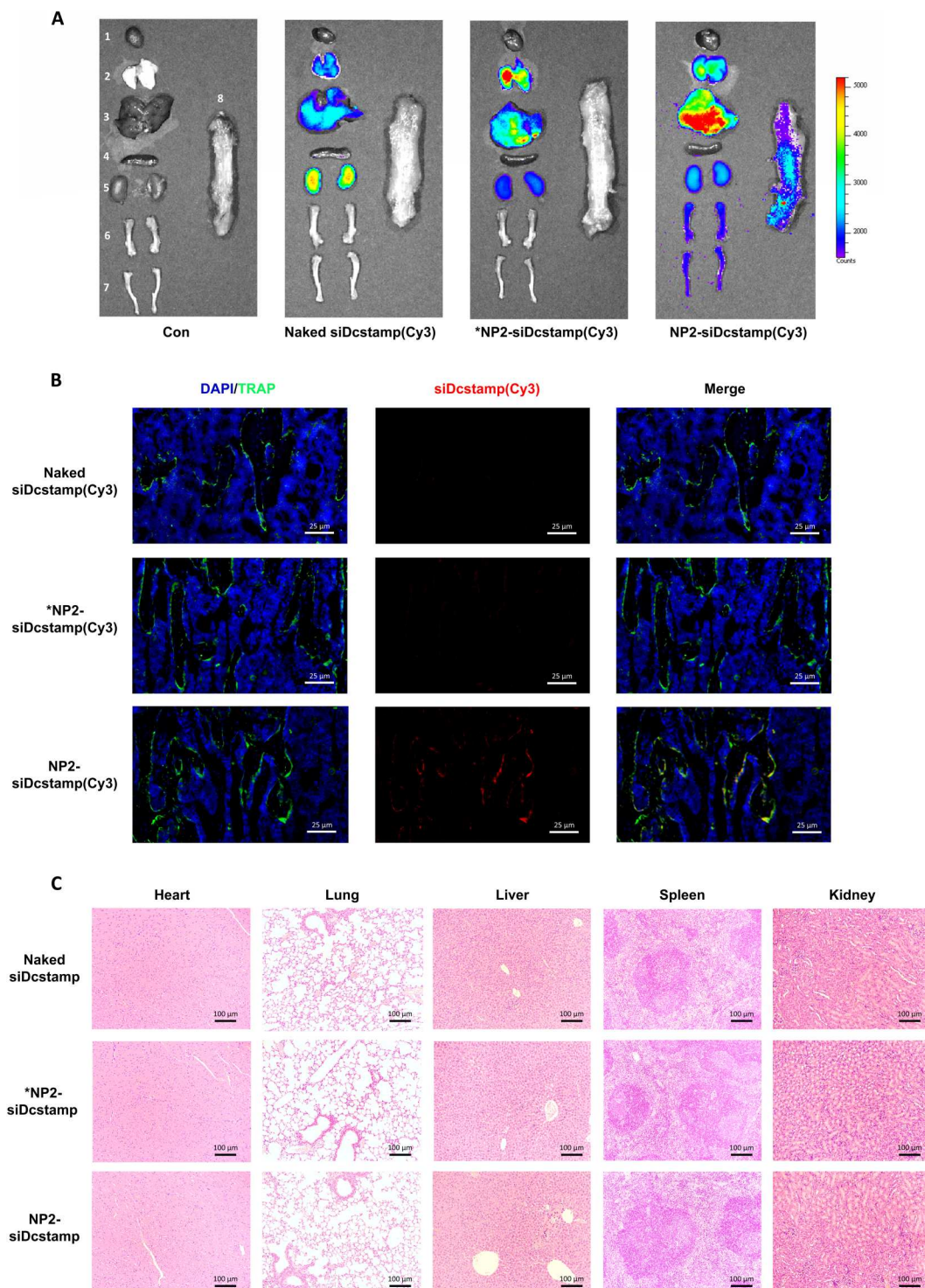
Fig. 7. Distribution and biocompatibility of NP-siDcstamp in vivo. (**A**) Tissue distribution of siDcstamp, *NP2-siNC, and NP2-siNC at 8 hours after injection: 1, heart; 2, lung; 3, liver; 4, spleen; 5, kidney; 6, femur; 7, tibias; 8, vertebrae. (**B**) Accumulation of siDcstamp on femoral bone surfaces from different groups. (**C**) Histological analysis of organ slices after the treatments indicated above. NP concentration was 1 mg/ml and 100 mg/kg in mice; $n = 4$ per group at all panels.
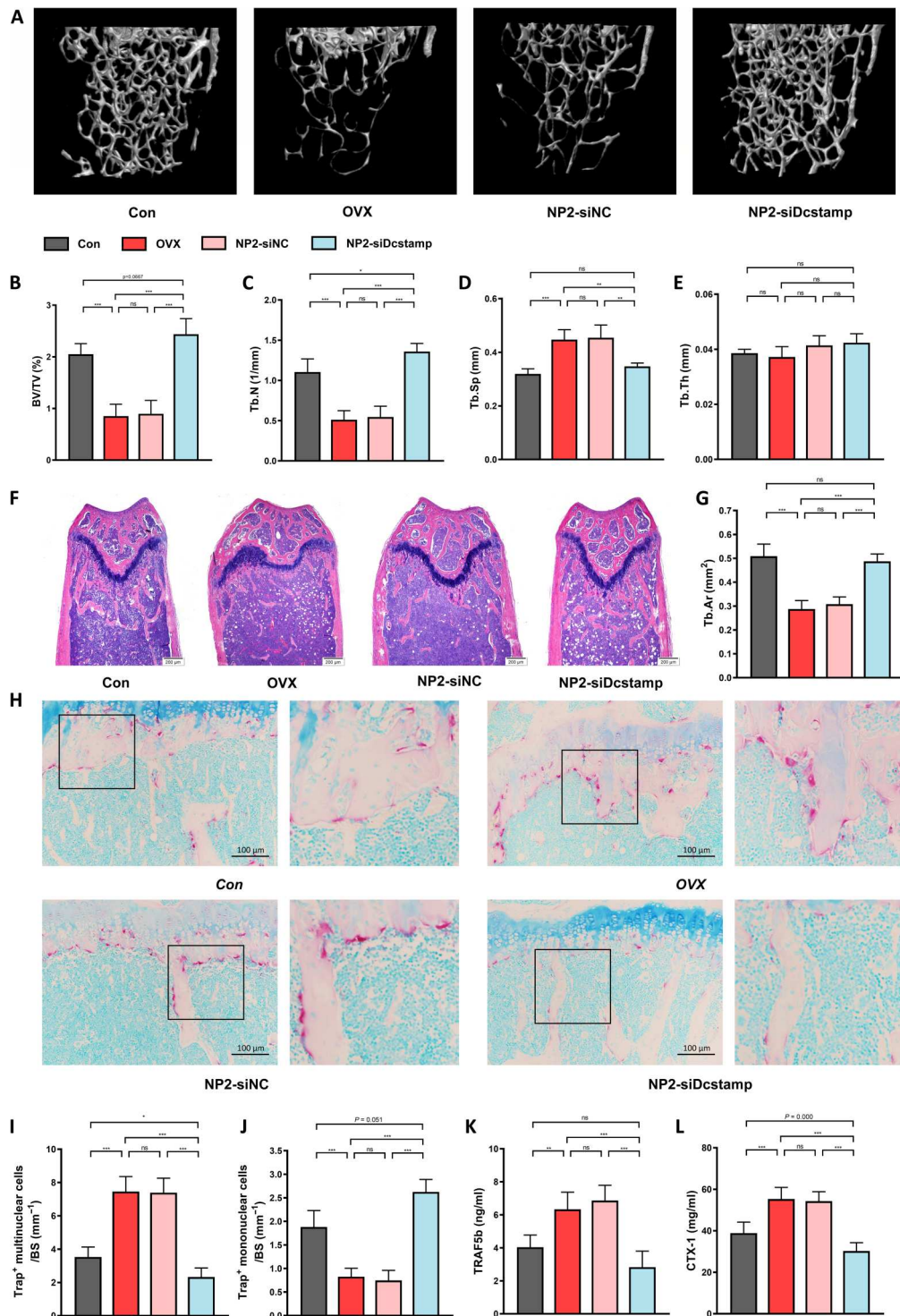
Fig. 8. NP2-siDcstamp prevents femoral trabecular bone loss in OVX mice. Administration of NP2-siNC and NP2-siDcstamp in OVX mice twice a week during 5 weeks. The concentration of NP2-siRNA was 1 mg/ml and 100 mg/kg in mice. (**A**) Reconstructed μCT images of distal femur. (**B** to **E**) Quantification of bone value/total value (BV/TV), trabecular number (Tb.N), trabecular space (Tb.Sp), and trabecular thickness (Tb.Th); $n = 6$ per group. (**F**) Representative H&E staining of distal femoral sections. (**G**) Quantification of the trabecular area (Tb.Ar) from H&E staining; $n = 6$ per group. (**H**) Representative TRAP-stained sections of the distal femur. (**I** and **J**) Quantification of Trap^{+} multinuclear cells (mature osteoclasts) (I) and Trap^{+} mononuclear cells (preosteoclasts) (J) from TRAP staining; $n = 4$ per group. (**K** and **L**) Serum levels of osteoclast markers: TRAP5b (K) and CTX-1 (L); $n = 5$ per group. Data are expressed as means ± SD. ns, no significance; *$P < 0.05$; **$P < 0.01$; ***$P < 0.001$.

increased after administration of NP2-siDcstamp (Fig. 8, F and G). These results validated the strong anti-osteoporotic effects of the transfected siDcstamp by bone-targeted NPs. Besides, the siDcstamp delivered by NP2 cross-linked by MBA (MBA-NP2-siDcstamp) did not improve OVX-induced bone loss, suggesting that GSH responsiveness of NPs is essential for the controlled release of siRNA (fig. S9). Note that the NP2-siDcstamp treatment barely interrupted the cortical parameters and trabecular thickness (Tb.Th; Fig. 8E and fig. S10).

We then explored the alterations of osteoclastogenesis after the treatment with NP2-siRNA complexes. TRAP staining revealed that the number of TRAP$^+$ multinuclear cells (osteoclasts) was enhanced in the OVX group, which was inhibited substantially by treatment with NP2-siDcstamp complexes (Fig. 8, H and I). In addition, TRAP$^+$ mononuclear cells (preosteoclasts) were clearly facilitated in the NP2-siDcstamp complex group (Fig. 8J). Consistently, the high serum levels of osteoclast markers including TRAP isoform 5b (TRAP5b) and C-telopeptide of type I collagen (CTX-1) in OVX mice were down-regulated by NP2-siDcstamp complexes (Fig. 8, K and L). Note that, upon treatment with NP2-siNC complexes, neither the inhibition of osteoclasts nor the promotion of preosteoclasts was found.

We further investigated whether NP2-siDcstamp is beneficial for promotion of bone formation and vascularization in femurs of OVX mice. Quantitative analysis using immunohistochemistry showed that, in the OVX group, the quantity of OCN$^+$ cells (osteoblasts) around femoral trabecula declined (Fig. 9, A and B). Calcein staining also revealed that mineral apposition rate (MAR) and bone formation rate per unit of bone surface (BFR/BS) decreased in OVX mice, suggesting a diminished osteogenesis due to estrogen deficiency (Fig. 9, C to E). The impairment in osteogenesis and bone formation was restored by NP2-siDcstamp with an even higher level of MAR compared with the control group (Fig. 9, C to E). The decreased serum markers for osteoblast function including procollagen I N-terminal propeptide and OCN in the OVX group were reversed as well by the NP2-siDcstamp treatment (Fig. 9, F and G). Type H vessels (CD31^{hi}Emcn^{hi}), which are essential for normal bone remodeling and initiation of new bone formation, are enriched adjacent to the growth plate (37). Preosteoclasts can induce angiogenesis of type H vessels by secreting PDGF-BB (8). In accord with previous studies (9, 38), microphil-perfused angiography showed that the femoral vessel volume decreased in the OVX group (Fig. 9, H and I). Immunofluorescence and flow cytometry also demonstrated that the quantity of type H vessels declined notably in OVX-induced bone loss model (Fig. 9, J to M). All these negative effects were suppressed substantially after the treatment with NP2-siDcstamp, which was not found with NP2-siNC (Fig. 9, H to M).

An earlier study found that alendronate performed well as bone targeting group and led to accumulation of drugs on both long bones and vertebrae (16). Our IVIS results (Fig. 7) also showed the enrichment of siRNA on femur and vertebrae. We therefore further investigated the therapeutic effects of NP2-siDcstamp on vertebrae in OVX mice. The findings were consistent with the femoral results; the decreased bone volume fraction and vertebral Tb.Th in OVX mice were reversed by the NP2-siDcstamp treatment (Fig. 10, A, B, and E). Although vertebral trabecular structural parameters including Tb.N and Tb.Sp did not change noticeably after OVX, the NP2-siDcstamp treatment led to slight, yet nonnegligible

improvements (Fig. 10, C and D). In addition, NP2-siDcstamp triggered decreased osteoclast number and preserved preosteoclasts (Fig. 10, F to K). These findings implied that NP2-siDcstamp can prevent OVX-induced bone loss by inhibiting preosteoclast fusion and simultaneously augment osteogenesis and angiogenesis.

DISCUSSION

Therapy based on RNA is a promising strategy for treating bone diseases, while the intrinsic problems with naked RNA restrict the therapy efficiency, which can be addressed by functional delivery vehicles. De La Vega et al. (39) reported that a chemically modified mRNA encoding BMP-2 could substantially promote bone regeneration locally. Xue et al. (40) developed a bisphosphonate lipid-like material to deliver mRNA into the bone microenvironment. Despite these pioneering achievements, most of the established delivery platforms suffer from different limitations on satisfied RNA delivery. For example, chemical modification of RNA requires precise molecular design and reaction control (41). The widely applied lipid NPs need to further enhance their structural stability, loading capacity, and delivery efficiency (42). Therefore, designing rational delivery vehicles that achieve sufficient RNA delivery remains desirable. We here developed a type of core-shell polyelectrolyte NP with the following features: a cationic and soft core for loading and protection of anionic siRNA, a biocompatible PEG shell for long circulation (stealth behavior) tagged with alendronate for bone-targeted delivery, and a redox-responsive cross-linker enabling glutathione-triggered release of siRNA.

We demonstrate that this platform successfully realizes transfection of an active siRNA (siDcstamp), thereby silencing Dcstamp mRNA in BMMs/preosteoclasts in vitro and subsequently causing the blocking of cell-cell fusion and osteoclastogenesis, as well as the promotion of osteogenesis and angiogenesis via PDGF-BB. Alendronate conjugated to the PEG blocks leads to enrichment of siDcstamp at bone surfaces and efficient transfection of preosteoclasts. In vivo experiments validated that siDcstamp transfection substantially attenuated OVX-induced trabecular bone loss not only by impeding bone resorption but also by augmenting bone formation and vascularization. We hope that our platform and the therapeutic achievements that we report will inspire even better designs of siRNA transfection vehicles and so lead to innovative strategies toward regulating preosteoclasts as anabolic treatment for osteoporosis and other osteoblast-induced bone diseases.

MATERIALS AND METHODS
Synthesis of polyelectrolyte NPs

Typically, PEG-CTA (4.00 mg), METAC (8.3 mg, 0.04 mmol), PAA (2.9 mg, 0.04 mmol), BAC (2.1 mg, 8.0×10^{-3} mmol), HMP (2-hydroxy-2-methyl-1-propanone, 0.1 mg, 8.00×10^{-4} mmol), and NaCl (3.5 mg, 0.06 mmol) were dissolved in 2-ml water. The pH of the solution was adjusted to 6.5. The tube was sealed and de-oxygenated by three freeze-vacuum-thaw cycles in nitrogen atmosphere. Then, the tube was exposed to UV light for 3 hours. The NPs were separated from the template by centrifugation using 1.5 M NaCl as eluent for three times with an Amicon Ultra centrifugal filter (Millipore; molecular weight cutoff = 100 kDa) followed by dialyzing against water to remove the salt. Alendronate-decorated core-shell polyelectrolyte NPs were synthesized as abovementioned
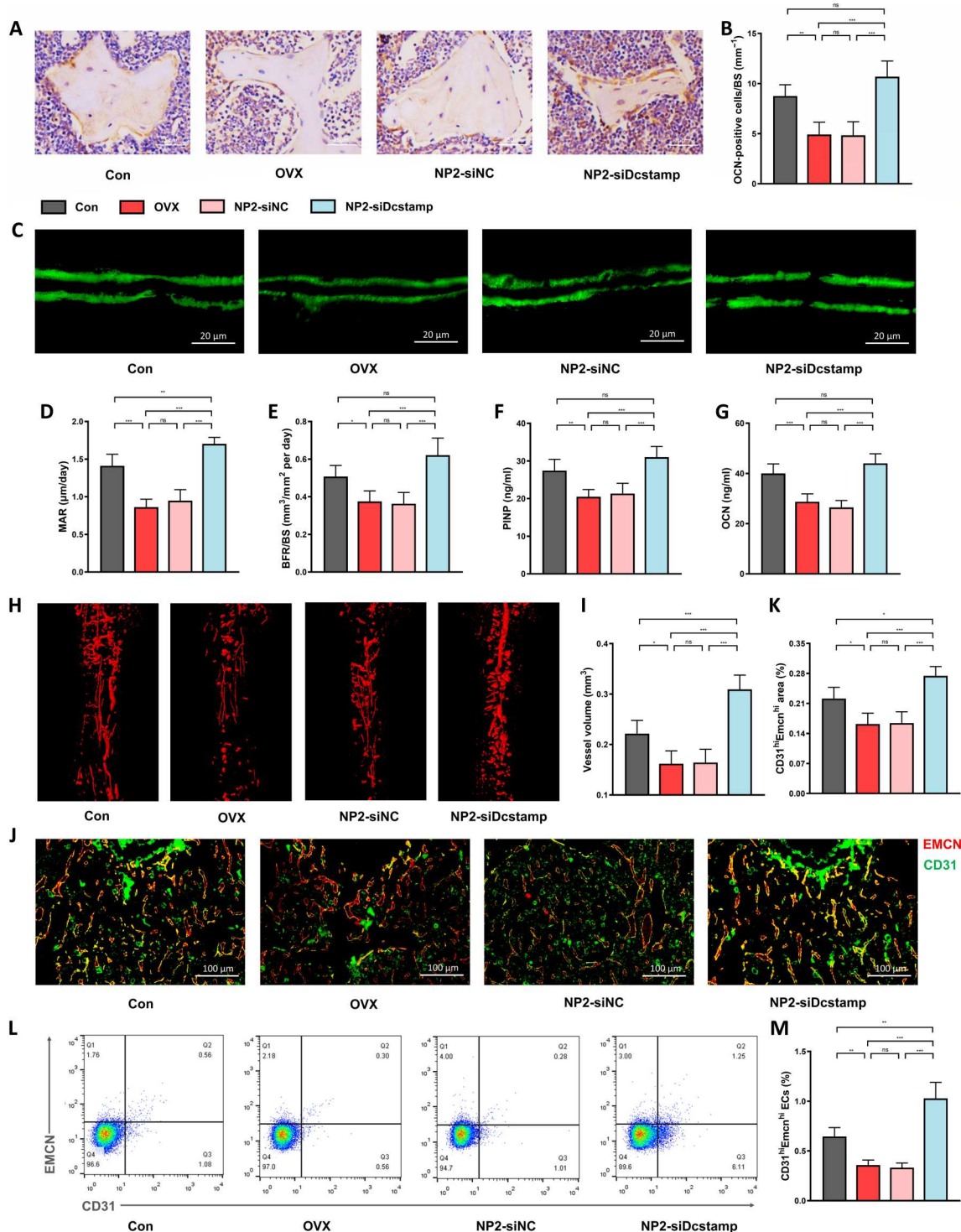
Fig. 9. NP2-siDcstamp promotes femoral bone formation and vascularization in OVX mice. (**A**) OCN-stained sections of the distal femur. (**B**) Quantification of OCN^{+} cells (osteoblasts) from OCN immunohistochemical images; *n* = 4 per group. (**C**) Representative calcein staining of trabecula of distal femoral sections. (**D** and **E**) Quantification analysis of calcein staining. Mineral apposition rate (MAR) (D) and bone formation rate per unit of bone surface (BFR/BS) (E); *n* = 5 per group. (**F** and **G**) Serum levels of osteoblast markers: procollagen I N-terminal propeptide (PINP) (F) and OCN (G); *n* = 5 per group. (**H**) Representative angiographic images of femora. (**I**) Quantification of vessel volume from angiography; *n* = 5 per group. (**J**) Representative images of immunostaining of EMCN (red), CD31 (green), and Emcn^hiCD31^hi (yellow) cells on trabecular bone. (**K**) Quantification of CD31^hiEmcn^hi area on trabecular bone from immunostaining images; *n* = 4 per group. (**L** and **M**) Flow cytometry plots with the percentage of CD31^hiEmcn^hi endothelial cells in total bone marrow cells; *n* = 4 per group. Data are expressed as means ± SD. ns, no significance; *$P < 0.05$; **$P < 0.01$; ***$P < 0.001$.
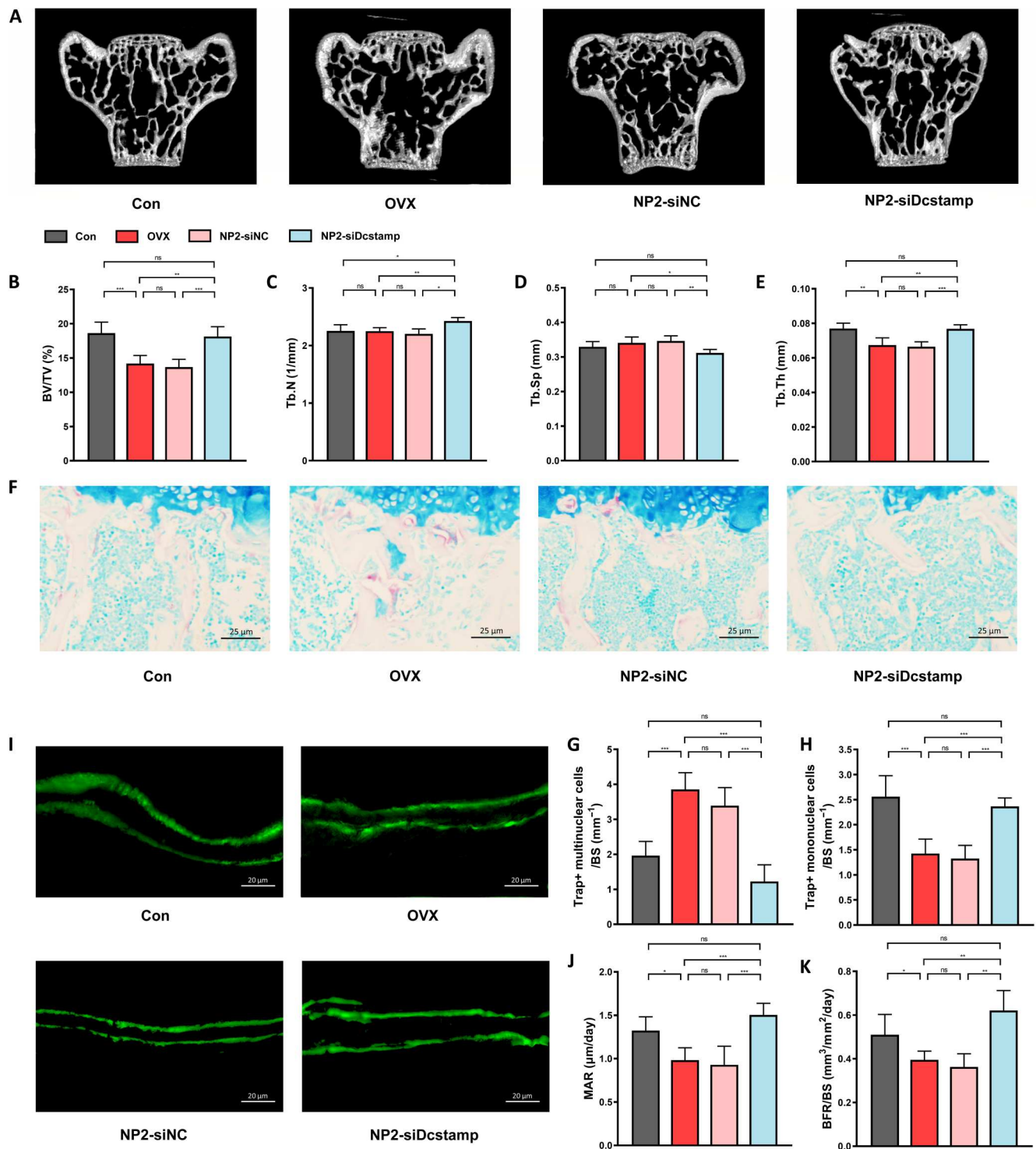
Fig. 10. NP2-siDcstamp prevents vertebral trabecular bone loss in OVX mice. (**A**) Reconstructed μCT images of vertebrae. (**B** to **E**) Quantification of BV/TV, Tb.N, Tb.Sp, and Tb.Th; $n = 5$ per group. (**F**) Representative TRAP-stained sections of the distal femur. (**G** and **H**) Quantification of Trap^{+} multinuclear cells (mature osteoclasts) (G) and Trap^{+} mononuclear cells (preosteoclasts) (H) from TRAP staining; $n = 4$ per group. (**I**) Representative calcein staining of trabecula of distal vertebral sections. (**J** and **K**) Quantification analysis of calcein staining. MAR (J) and BFR/BS (K); $n = 5$ per group. Data are expressed as means ± SD. ns, no significance; *$P < 0.05$; **$P < 0.01$; ***$P < 0.001$.

method using alendronate-modified AD-PEG-CTA. The "bare" PMETAC NPs (no PEG shell) were synthesized according to a previous report (27).

For conjugation with siRNA, NPs were mixed with siRNA in culture medium/DEPC (diethyl pyrocarbonate) water/sterile saline and incubated for about 3 min. Then, the medium was added into cultured cells.

Characterization of polyelectrolyte NPs

NPs were mixed with siRNA in DEPC water and then incubated for 3 min to let them conjugate spontaneously. The binding capacity was then evaluated by agarose gel electrophoresis as previously reported (43, 44). NP-siRNA complexes were prepared with weight ratio from 1:1 to 80:1 (NP/siRNA; w/w) and then mixed with DNA loading buffer (10×). The mixture was loaded onto a 2.5% agarose gel (with GelRed) and subjected to electrophoresis at 40 V for 30 min. Then, RNAs were analyzed by an UV illuminator. For the serum stability assay, the naked siRNA, NP-siDcstamp complexes were incubated with 50% FBS for 1 to 48 hours. Isoquants from every sample were mixed with loading buffer and loaded on 2.5% gel. Then, the electrophoresis was run at 130 V for 30 min and RNA was analyzed on an UV illuminator.

Isolation of primary mouse BMMs and osteoclastic differentiation assay

Osteoclastic differentiation of primary BMMs was reported previously (45). Briefly, the femurs and tibias of 6-week-old mice were collected, cleared, and placed in the sectioned tips within the centrifuge tubes after both the proximal and distal ends were made small cuts. Then, the tubes were centrifuged at 10,000g for 15 s at room temperature and flushed bone marrow was suspended in the normal medium consisting of α-MEM (minimum essential medium) with 10% FBS and 1% penicillin/streptomycin. After 24 hours of mixed culture, the culture medium was removed, nonadherent cells were collected, cells were seeded in 24-well or 12-well plates after ammonium-chloride-potassium (ACK) lysing buffer, and then the induction of osteoclast differentiation began by normal medium with M-CSF (30 ng/ml) and RANKL (80 ng/ml) for 5 days (fig. S11A).

For siRNA transfection during osteoclastogenesis, NPs were mixed with siRNA at a weight ratio of 20:1 and the complexes were added to cells on day 2 after the beginning of RANKL stimulation. For example, for preparation of NP-siRNA complexes (20 μg/ml), 4 μl of NP storage solution (5 mg/ml) and 4 μl of siRNA storage solution (20 μM) were mixed in 200 μl of fresh cell culture medium and incubated for 3 min at room temperature. Then, 200 μl of NP-siRNA mixture was added to a well of 12-well plate with 800 μl of fresh culture medium at day 2 of osteoclastogenesis induction. After incubation for 24 hours, the plates were changed to fresh medium (fig. S11A).

In vitro assay for osteoclast fusion and function

Pit formation assay was performed using biomimetic synthetic bone plate (Corning) as previously described (46). Briefly, BMMs were induced into mature osteoclasts by M-CSF (30 ng/ml) and RANKL (80 ng/ml), which were digested and seeded on hydroxyapatite-coated surfaces for another 2-day culture. Then, images were obtained with a microscope and analyzed by Image-Pro Plus software.

Osteoclast fusion assay was carried out as previously reported (38). Briefly, primary BMMs were induced by M-CSF (30 ng/ml) and RANKL (80 ng/ml) for 3 days and then labeled with Hoechst or CM-Dil for 20 min at room temperature (fig. S11B). Then, two groups of cells were cultured together for 12 hours and photos were taken by fluorescence microscopy (fig. S11B).

BMSC/BMM and EPC/BMM coculture system in vitro

Primary BMSCs were isolated from the bone marrow of C57 mice as we described before (45, 47). Then, primary BMSCs and BMMs were seeded in the top and bottom chamber of 12-well 0.4-μm transwell plate and cultured in osteogenic medium (normal medium containing 10 mM β-glycerophosphate, 50 μM ascorbic acid, and 100 nM dexamethasone) with or without M-CSF (30 ng/ml) and RANKL (50 ng/ml) for 6 days. Then, cells were harvested for different experiments (Fig. 5A and fig. S3A).

Primary EPCs were isolated from mice peripheral blood as previously reported (48). BMMs were cultured in osteoclastic medium [with M-SCF (30 ng/ml) and RANKL (80 ng/ml)] or normal medium for 5 days. The transfection of siRNA was performed on day 2 of osteoclastogenesis induction. Then, we collected the osteoclast medium and mixed with normal culture medium at a ratio of 1:2 as CM to culture EPCs for further investigations (Fig. 6A and fig. S4A).

Gene expression analysis

The transcriptional expression level was measured by RT-qPCR as we previously reported (49). Total RNA was extracted using an RNA quick purification kit, and complementary DNA was obtained by using the PrimeScript RT Reagent Kit. Then, RT-qPCR was performed using TB Green reagent on the ABI PRISM 7900HT System (Applied Biosystems, Foster City, USA). Primers used in this study were listed in table S2.

The protein expression levels were evaluated by Western blot as we previously described (49). The primary antibodies used in this study were anti-CTSK, anti-MMP9, anti-NFATc1, anti-CAR2, anti-DCSTAMP, anti-RUNX2, anti-ALP, anti-OCN, and anti–PDGF-BB (detailed information listed in "Materials" section of Supplementary Materials).

OVX model and treatments in vivo

All procedures on animals were abided by the guidelines of the Ethics Committee on Animal Experiments of Changzheng Hospital, affiliated to Naval Medical University. C57BL/6 mice were purchased from Shanghai Jihui Laboratory Animal Care Co. (Shanghai, China) and kept under specific pathogen–free conditions at Animal Experimental Center of Naval Medical University (SYXK 2017-0004). Eight-week-old female mice were randomly divided into four groups. NPs were mixed with siRNA at a weight ratio of 20:1, then diluted in normal saline (final concentration: 5 mg/ml), and injected intravenously twice a week at a dose of 100 mg/kg (0.2 ml for 20 g). The weight of mice was measured once a week. Sham group: mice received sham surgery with normal saline; OVX group: mice received OVX surgery with normal saline; NP2-siNC: mice received sham surgery and NP2 (with siNC) treatment; NP2-siDcstamp: mice received sham surgery and NP2 (with siDcstamp) treatment. The detailed protocols for OVX model or sham surgery were described previously (50).

µCT analysis

The collected femurs and vertebrae were fixed in 4% paraformaldehyde for 24 hours. Then, the structure and microarchitecture of distal femur and the second lumbar spinal vertebra (L2) were analyzed by high-resolution µCT (SkyScan 1076, Bruker) at a resolution of 8 µm per pixel, a voltage of 80 kV, and a current of 124 µA. Then, trabecular parameters including bone volume/total volume (BV/TV; %), trabecular number (Tb.N; 1/mm), trabecular space (Tb.Sp; mm), trabecular thickness (Tb.Th; mm), and trabecular bone mineral density (Tb.BMD; g/cm^3) and cortical parameters including cross-sectional cortical bone area (Ct.Ar; mm^2) and cortical thickness (Ct.Th; mm) were obtained by CTAn and CTVol.

Histological and immunofluorescence analysis

Femurs and vertebrae were fixed in 4% paraformaldehyde for 48 hours and decalcified in 15% tetrasodium EDTA for 4 weeks. Then, tissues were dehydrated overnight, embedded in paraffin, and sectioned at 5 µm thick for hematoxylin and eosin staining, TRAP staining, OCN immunohistochemistry, and CD31 and endomucin (EMCN) immunofluorescence. Images were acquired by fluorescence microscopy (Nikon) with a digital Olympus camera and analyzed by Image-Pro Plus software.

Flow cytometry

$CD31^{hi}EMCN^{hi}$ cells in the femur and tibia were measured by flow cytometry as previously described (38). Briefly, we dissected the bones, made small cuts at both sides, and placed them in the sectioned tips within the centrifuge tubes. Then, the tubes were centrifuged at $10,000g$ for 15 s to get whole bone marrow cells. After ACK lysis, cells were incubated with phycoerythrin/Cy7 anti-mouse CD31 antibody (BioLegend), EMCN monoclonal antibody (eBioscience), fluorescein isothiocyanate (FITC) anti-mouse TER-119/erythroid cell antibody (BioLegend), and FITC anti-mouse CD45 antibody (BioLegend). Cell sorting was performed with CyAn ADP Analyzer (Beckman Coulter), and $CD31^+CD45^-Ter119^-$ cells were considered bone marrow endothelial cells.

Angiography

The femoral blood vessels were measured by µCT as previously reported (36). Briefly, mice were euthanized, the thoracic cavity was opened, a cut was made on the auricula dextra, and a needle was inserted into the left ventricle. Then, the entire vasculature was perfused with 9 ml of warm heparinized saline (100 U/ml in 0.9% saline), 9 ml of 4% paraformaldehyde, another 9 ml of warm heparinized saline, and then 5 ml of Microfil MV-122 (Flow Tech). Next, the femurs were removed and fixed for the detection of µCT.

Statistical analyses

All data are expressed as means ± SE of at least three repetitions. The one-way analysis of variance (ANOVA) followed by Student-Newman-Keuls post hoc tests was used to compare multiple groups by GraphPad Prism software. Differences were considered significant at $*P < 0.05$, $**P < 0.01$, and $***P < 0.001$.

Supplementary Materials

This PDF file includes:
Supplementary Materials and Methods
Tables S1 and S2

Figs. S1 to S11
References

View/request a protocol for this paper from *Bio-protocol*.

REFERENCES AND NOTES

1. Y. Peng, S. Wu, Y. Li, J. L. Crane, Type H blood vessels in bone modeling and remodeling. *Theranostics* **10**, 426–436 (2020).
2. J. Tuckermann, R. H. Adams, The endothelium-bone axis in development, homeostasis and bone and joint disease. *Nat. Rev. Rheumatol.* **17**, 608–620 (2021).
3. Y. Xiao, C. S. McGuinness, W. S. Doherty-Boyd, M. Salmeron-Sanchez, H. Donnelly, M. J. Dalby, Current insights into the bone marrow niche: From biology in vivo to bioengineering ex vivo. *Biomaterials* **286**, 121568 (2022).
4. I. R. Reid, E. O. Billington, Drug therapy for osteoporosis in older adults. *Lancet* **399**, 1080–1092 (2022).
5. L. L. Chang, R. Eastell, P. D. Miller, Continuation of bisphosphonate therapy for osteoporosis beyond 5 years. *N. Engl. J. Med.* **386**, 1467–1469 (2022).
6. Pharmacotherapy for postmenopausal osteoporosis. *JAMA* **325**, 1888–1889 (2021).
7. J. R. Edwards, G. R. Mundy, Advances in osteoclast biology: Old findings and new insights from mouse models. *Nat. Rev. Rheumatol.* **7**, 235–243 (2011).
8. H. Xie, Z. Cui, L. Wang, Z. Xia, Y. Hu, L. Xian, C. Li, L. Xie, J. Crane, M. Wan, G. Zhen, Q. Bian, B. Yu, W. Chang, T. Qiu, M. Pickarski, L. T. Duong, J. J. Windle, X. Luo, E. Liao, X. Cao, PDGF-BB secreted by preosteoclasts induces angiogenesis during coupling with osteogenesis. *Nat. Med.* **20**, 1270–1278 (2014).
9. C. Dou, N. Ding, F. Luo, T. Hou, Z. Cao, Y. Bai, C. Liu, J. Xu, S. Dong, Graphene-based microRNA transfection blocks preosteoclast fusion to increase bone formation and vascularization. *Adv. Sci.* **5**, 1700578 (2018).
10. C. Dou, C. Zhang, F. Kang, X. Yang, H. Jiang, Y. Bai, J. Xiang, J. Xu, S. Dong, MiR-7b directly targets DC-STAMP causing suppression of NFATc1 and c-Fos signaling during osteoclast fusion and differentiation. *Biochim. Biophys. Acta* **1839**, 1084–1096 (2014).
11. Y. Zhuang, W. Cui, Biomaterial-based delivery of nucleic acids for tissue regeneration. *Adv. Drug Deliv. Rev.* **176**, 113885 (2021).
12. J. K. Lam, M. Y. Chow, Y. Zhang, S. W. Leung, siRNA versus miRNA as therapeutics for gene silencing. *Mol. Ther. Nucl. Acids* **4**, e252 (2015).
13. R. L. Setten, J. J. Rossi, S. P. Han, The current state and future directions of RNAi-based therapeutics. *Nat. Rev. Drug Discov.* **18**, 421–446 (2019).
14. M. R. Reagan, D. L. Kaplan, Concise review: Mesenchymal stem cell tumor-homing: Detection methods in disease model systems. *Stem Cells* **29**, 920–927 (2011).
15. D. W. Malcolm, Y. Wang, C. Overby, M. Newman, D. S. W. Benoit, Delivery of RNAi-based therapeutics for bone regeneration. *Curr. Osteoporos. Rep.* **18**, 312–324 (2020).
16. J. Hoque, Y. V. Shih, Y. Zeng, H. Newman, N. Sangaj, N. Arjunji, S. Varghese, Bone targeting nanocarrier-assisted delivery of adenosine to combat osteoporotic bone loss. *Biomaterials* **273**, 120819 (2021).
17. L. Ma, W. Ke, Z. Liao, X. Feng, J. Lei, K. Wang, B. Wang, G. Li, R. Luo, Y. Shi, W. Zhang, Y. Song, W. Sheng, C. Yang, Small extracellular vesicles with nanomorphology memory promote osteogenesis. *Bioact. Mater.* **17**, 425–438 (2022).
18. S. Gangopadhyay, K. R. Gore, Advances in siRNA therapeutics and synergistic effect on siRNA activity using emerging dual ribose modifications. *RNA Biol.* **19**, 452–467 (2022).
19. R. Titze-de-Almeida, C. David, S. S. Titze-de-Almeida, The race of 10 synthetic RNAi-based drugs to the pharmaceutical market. *Pharm. Res.* **34**, 1339–1363 (2017).
20. C. Shi, T. Wu, Y. He, Y. Zhang, D. Fu, Recent advances in bone-targeted therapy. *Pharmacol. Ther.* **207**, 107473 (2020).
21. H. Yang, Q. Wang, S. Huang, A. Xiao, F. Li, L. Gan, X. Yang, Smart pH/redox dual-responsive nanogels for on-demand intracellular anticancer drug release. *ACS Appl. Mater. Interfaces* **8**, 7729–7738 (2016).
22. K. Søe, Osteoclast fusion: Physiological regulation of multinucleation through heterogeneity-potential implications for drug sensitivity. *Int. J. Mol. Sci.* **21**, 7717 (2020).
23. K. Fujita, M. Iwasaki, H. Ochi, T. Fukuda, C. Ma, T. Miyamoto, K. Takitani, T. Negishi-Koga, S. Sunamura, T. Kodama, H. Takayanagi, H. Tamai, S. Kato, H. Arai, K. Shinomiya, H. Itoh, A. Okawa, S. Takeda, Vitamin E decreases bone mass by stimulating osteoclast fusion. *Nat. Med.* **18**, 589–594 (2012).
24. J. Li, Y. Anraku, K. Kataoka, Self-boosting catalytic nanoreactors integrated with triggerable crosslinking membrane networks for initiation of immunogenic cell death by pyroptosis. *Angew. Chem. Int. Ed.* **59**, 13526–13530 (2020).
25. K. Achazi, R. Haag, M. Ballauff, J. Dernedde, J. N. Kizhakkedathu, D. Maysinger, G. Multhaup, Understanding the interaction of polyelectrolyte architectures with proteins and biosystems. *Angew. Chem. Int. Ed.* **60**, 3882–3904 (2021).

26. Y. Cai, P. Ding, J. Ni, L. Zhou, A. Ahmad, X. Guo, M. A. C. Stuart, J. Wang, Regulated polyelectrolyte nanogels for enzyme encapsulation and activation. *Biomacromolecules* **22**, 4748–4757 (2021).

27. P. Ding, J. Huang, C. Wei, W. Liu, W. Zhou, J. Wang, M. Wang, X. Guo, M. A. C. Stuart, J. Wang, Efficient and generic preparation of diverse polyelectrolyte nanogels by electrostatic assembly directed polymerization. *CCS Chem.* **2**, 1016–1025 (2020).

28. J. Ni, Y. Wan, Y. Cai, P. Ding, M. A. C. Stuart, J. Wang, Synthesis of anionic nanogels for selective and efficient enzyme encapsulation. *Langmuir* **38**, 3234–3243 (2022).

29. L. Zhou, Y. Gao, Y. Cai, J. Zhou, P. Ding, M. A. C. Stuart, J. Wang, Controlled synthesis of PEGylated polyelectrolyte nanogels as efficient protein carriers. *J. Colloid Interface Sci.* **620**, 322–332 (2022).

30. P. Ding, W. Liu, X. Guo, M. A. C. Stuart, J. Wang, Optimal synthesis of polyelectrolyte nanogels by electrostatic assembly directed polymerization for dye loading and release. *Soft Matter* **17**, 887–892 (2021).

31. Y. Liu, H. H. Winter, S. L. Perry, Linear viscoelasticity of complex coacervates. *Adv. Colloid Interface Sci.* **239**, 46–60 (2017).

32. Y. Liu, B. Momani, H. H. Winter, S. L. Perry, Rheological characterization of liquid-to-solid transitions in bulk polyelectrolyte complexes. *Soft Matter* **13**, 7332–7340 (2017).

33. R. Cheng, F. Feng, F. Meng, C. Deng, J. Feijen, Z. Zhong, Glutathione-responsive nanovehicles as a promising platform for targeted intracellular drug and gene delivery. *J. Control. Release* **152**, 2–12 (2011).

34. N. Ding, C. Liu, L. Yao, Y. Bai, P. Cheng, Z. Li, K. Luo, T. Mei, J. Li, J. Xing, X. Gao, Q. Ma, J. Xu, F. Luo, C. Dou, Alendronate induces osteoclast precursor apoptosis via peroxisomal dysfunction mediated ER stress. *J. Cell. Physiol.* **233**, 7415–7423 (2018).

35. J. Huang, H. Yin, S. S. Rao, P. L. Xie, X. Cao, T. Rao, S. Y. Liu, Z. X. Wang, J. Cao, Y. Hu, Y. Zhang, J. Luo, Y. J. Tan, Z. Z. Liu, B. Wu, X. K. Hu, T. H. Chen, C. Y. Chen, H. Xie, Harmine enhances type H vessel formation and prevents bone loss in ovariectomized mice. *Theranostics* **8**, 2435–2446 (2018).

36. C. Dou, J. Li, J. He, F. Luo, T. Yu, Q. Dai, Y. Chen, J. Xu, X. Yang, S. Dong, Bone-targeted pH-responsive cerium nanoparticles for anabolic therapy in osteoporosis. *Bioact. Mater.* **6**, 4697–4706 (2021).

37. M. Chen, Y. Li, X. Huang, Y. Gu, S. Li, P. Yin, L. Zhang, P. Tang, Skeleton-vasculature chain reaction: A novel insight into the mystery of homeostasis. *Bone Res.* **9**, 21 (2021).

38. X. Li, L. Wang, B. Huang, Y. Gu, Y. Luo, X. Zhi, Y. Hu, H. Zhang, Z. Gu, J. Cui, L. Cao, J. Guo, Y. Wang, Q. Zhou, H. Jiang, C. Fang, W. Weng, X. Chen, X. Chen, J. Su, Targeting actin-bundling protein L-plastin as an anabolic therapy for bone loss. *Sci. Adv.* **6**, eabb7135 (2020).

39. R. E. De La Vega, M. van Griensven, W. Zhang, M. J. Coenen, C. V. Nagelli, J. A. Panos, C. J. Peniche Silva, J. Geiger, C. Plank, C. H. Evans, E. R. Balmayor, Efficient healing of large osseous segmental defects using optimized chemically modified messenger RNA encoding BMP-2. *Sci. Adv.* **8**, eabl6242 (2022).

40. L. Xue, N. Gong, S. J. Shepherd, X. Xiong, X. Liao, X. Han, G. Zhao, C. Song, X. Huang, H. Zhang, M. S. Padilla, J. Qin, Y. Shi, M. G. Alameh, D. J. Pochan, K. Wang, F. Long, D. Weissman, M. J. Mitchell, Rational design of bisphosphonate lipid-like materials for mRNA delivery to the bone microenvironment. *J. Am. Chem. Soc.* **144**, 9926–9937 (2022).

41. S. Qin, X. Tang, Y. Chen, K. Chen, N. Fan, W. Xiao, Q. Zheng, G. Li, Y. Teng, M. Wu, X. Song, mRNA-based therapeutics: Powerful and versatile tools to combat diseases. *Signal Transduct. Target. Ther.* **7**, 166 (2022).

42. L. Sercombe, T. Veerati, F. Moheimani, S. Y. Wu, A. K. Sood, S. Hua, Advances and challenges of liposome assisted drug delivery. *Front. Pharmacol.* **6**, 286 (2015).

43. Y. Sun, X. Ye, M. Cai, X. Liu, J. Xiao, C. Zhang, Y. Wang, L. Yang, J. Liu, S. Li, C. Kang, B. Zhang, Q. Zhang, Z. Wang, A. Hong, X. Wang, Osteoblast-targeting-peptide modified nanoparticle for siRNA/microRNA delivery. *ACS Nano* **10**, 5759–5768 (2016).

44. S. Su, Y. Tian, Y. Li, Y. Ding, T. Ji, M. Wu, Y. Wu, G. Nie, "Triple-punch" strategy for triple negative breast cancer therapy with minimized drug dosage and improved antitumor efficacy. *ACS Nano* **9**, 1367–1378 (2015).

45. D. E. Maridas, E. Rendina-Ruedy, P. T. Le, C. J. Rosen, Isolation, culture, and differentiation of bone marrow stromal cells and osteoclast progenitors from mice. *J. Vis. Exp.* **131**, 56750 (2018).

46. A. Vesprey, W. Yang, Pit assay to measure the bone resorptive activity of bone marrow-derived osteoclasts. *Bio-protocol* **6**, e1836 (2016).

47. M. Soleimani, S. Nadri, A protocol for isolation and culture of mesenchymal stem cells from mouse bone marrow. *Nat. Protoc.* **4**, 102–106 (2009).

48. C. J. Loomans, H. Wan, R. de Crom, R. van Haperen, H. C. de Boer, P. J. Leenen, H. A. Drexhage, T. J. Rabelink, A. J. van Zonneveld, F. J. Staal, Angiogenic murine endothelial progenitor cells are derived from a myeloid bone marrow fraction and can be identified by endothelial NO synthase expression. *Arterioscler. Thromb. Vasc. Biol.* **26**, 1760–1767 (2006).

49. Z. Zhang, T. Lin, Y. Meng, M. Hu, L. Shu, H. Jiang, R. Gao, J. Ma, C. Wang, X. Zhou, FOS/GOS attenuates high-fat diet induced bone loss via reversing microbiota dysbiosis, high intestinal permeability and systemic inflammation in mice. *Metabolism* **119**, 154767 (2021).

50. V. R. Souza, E. Mendes, M. Casaro, A. Antiorio, F. A. Oliveira, C. M. Ferreira, Description of ovariectomy protocol in mice. *Methods Mol. Biol.* **1916**, 303–309 (2019).

51. D. E. Koppel, Analysis of macromolecular polydispersity in intensity correlation spectroscopy: The method of cumulants. *J. Chem. Phys.* **57**, 4814 (1972).

52. S. W. Provencher, Contin: A general purpose constrained regularization program for inverting noisy linear algebraic and integral equations. *Comput. Phys. Commun.* **27**, 229–242 (1982).

53. S. W. Provencher, A constrained regularization method for inverting data represented by linear algebraic or integral equations. *Comput. Phys. Commun.* **27**, 213–227 (1982).

54. C. C. Liang, A. Y. Park, J. L. Guan, In vitro scratch assay: A convenient and inexpensive method for analysis of cell migration in vitro. *Nat. Protoc.* **2**, 329–333 (2007).

55. Y. Ding, M. Cai, Z. Cui, L. Huang, L. Wang, X. Lu, Y. Cai, Synthesis of low-dimensional polyion complex nanomaterials via polymerization-induced electrostatic self-assembly. *Angew. Chem. Int. Ed.* **57**, 1053–1056 (2018).

56. Q. Yu, Y. Ding, H. Cao, X. Lu, Y. Cai, Use of polyion complexation for polymerization-induced self-assembly in water under visible light irradiation at 25 °C. *ACS Macro Lett.* **4**, 1293–1296 (2015).